Supplementary Information
Evolution from a charge-ordered insulator to a high-temperature superconductor in $Bi_2Sr_2(Ca,Dy)Cu_2O_{8+\delta}$

Changwei Zou,[1,2] Jaewon Choi,[3] Qizhi Li,[1,4] Shusen Ye,[2] Chaohui Yin,[5] Mirian Garcia-Fernandez,[3] Stefano Agrestini,[3] Qingzheng Qiu,[1] Xinqiang Cai,[1] Qian Xiao,[1] Xingjiang Zhou,[5] Ke-Jin Zhou,[3] Yayu Wang,[2,6] and Yingying Peng[1,7]

[1] *International Center for Quantum Materials, School of Physics, Peking University, Beijing 100871, China*
[2] *State Key Laboratory of Low Dimensional Quantum Physics,*
Department of Physics, Tsinghua University, Beijing 100084, China
[3] *Diamond Light Source, Harwell Campus, Didcot, UK*
[4] *Present Address: Shenzhen Pinghu Laboratory, Building C, Chinese Sciences Vally,*
Industrial Park (iBT), Pinghu Street Longgang District, Shenzhen, 518111, China
[5] *Beijing National Laboratory for Condensed Matter Physics,*
Institute of Physics, Chinese Academy of Sciences, Beijing 100190, China
[6] *Frontier Science Center for Quantum Information, Beijing 100084, China*
[7] *Collaborative Innovation Center of Quantum Matter, Beijing 100871, China*
(Dated: August 12, 2024)

This PDF file includes:
Supplementary Notes
Supplementary References
Supplementary Figures 1 to 11

SUPPLEMENTARY NOTES

1. Characterizations of the Dy-Bi2212 samples

The growing and annealing conditions for our Dy-Bi2212 samples have been described in the Methods section of the main text. Before the RIXS and STM measurements, the samples were characterized by magnetic susceptibility as shown in Supplementary Fig. 1a. The as-grown sample (black) shows a broad superconducting transition with an onset of $T_c = 40$ K, corresponding to $p = 0.067\pm0.008$ (the error is obtained by considering the transition width) according to an empirical formula (see ref. [1]). We note that, in principle, the T_c^{max} within the formula should correspond to that of Dy-Bi2212. However, the Dy substitutions are introduced for severe underdoping, and references for "optimally" doping Dy0.4-Bi2212 are unavailable. Therefore, the T_c^{max} is set to 96 K as suggested by [1], for our hole concentration estimation. Although the T_c^{max} varies in different reports, it is important to note its precise value does not affect our main conclusions. The estimated doping level will exhibit only minimal variation when different T_c^{max} values are considered. For instance, in the case of Bi2212 with $T_c = 20$ K, the calculated doping level is approximately $p = 0.0619$ for $T_c^{max} = 98$ K, $p = 0.0621$ for $T_c^{max} = 96$ K, and $p = 0.0628$ for $T_c^{max} = 91$ K. The essential finding of our work lies in two dopings across the onset of the superconducting dome ($p = 0.05$): one is insulating, and the other is superconducting with $T_c = 20$ K. The precise value of T_c^{max} does not alter this fundamental aspect.

In the present study, we obtained two more underdoped samples by post-annealing, one superconducting with $p = 0.062\pm0.006$ (red, Ann1) and the other insulating with $p = 0.04\pm0.01$ where no signature of SC is observed (blue, Ann2). The four-probe resistance-*vs*-temperature curve in Supplementary Fig. 1b was obtained on another sample in the same batch as the $p \sim 0.04$ one. Supplementary Fig. 1a shows that the SC transition is generally broad in underdoped cuprates. There are two main reasons. The first one is owing to the difficulty in annealing severely underdoped Bi2212. The second reason is that compared to the doping range close to the top of the SC dome, the T_c vs. p trend is much steeper near the dome edge, which means that an equal uncertainty range of p will lead to a broader distribution of T_c in this regime.

Before the RIXS measurements, we collected the X-ray absorption spectra (XAS) on the two Dy-Bi2212 samples, as shown in Supplementary Fig. 1c. Then, we tuned the incident photon energy to the Cu L_3-edge maximum at 928.7 eV for our RIXS measurements. The XAS spectra were taken by measuring total electron yield with normal incident angle, which are also used for self-absorption correction of the RIXS data. Note that the spectra are virtually identical in the $p = 0.06$ and $p = 0.04$ samples, reflecting their similar hole concentrations. However, the ground states are different (one insulating, the other superconducting); for example, the magnitude of PG has shrunk significantly

in the $p = 0.06$ sample (see Supplementary Fig. 6). Because T_c might differ for different pieces before annealing in the same batch. To avoid such issues, we have used the same as-grown sample (black in Supplementary Fig. 1a) for further annealing. By dividing this sample into two smaller pieces, we have obtained the $p = 0.06$ (Ann1) and $p = 0.04$ (Ann2) samples in the manuscript. Notably, the STM measurements were carried out in the very same samples after the RIXS experiments.

2. Charge order revealed by the raw data and its intertwining with PG

Supplementary Fig. 2 displays the raw RIXS data (corrected for self-absorption effect) with varied temperatures and dopings. Similar to Fig. 2 of the main text, the lower panel of each figure is the integrated intensity profile over the quasi-elastic region. The data unambiguously reveal that the CO has already existed at temperatures as high as 273 K in both samples. The CO gradually becomes stronger with cooling but remains short-ranged. Due to the thermal broadening effect (as a rough estimation, $k_B T \sim 24$ meV at $T = 273$ K), the quasi-elastic region has an overall higher intensity at higher temperatures.

Supplementary Fig. 3 shows the bias voltage dependence of the dI/dV maps of both samples, revealing the non-dispersive nature of the real-space CO pattern. We note that the DOS modulation still exists at Fermi energy (0 meV), reflecting the finite zero-bias DOS for the PG spectra (e.g., Fig. 1d of the main text). This feature strengthens the idea that CO is a modulation of charge density, which is expected to involve DOS at the Fermi energy. We note that the previous study (ref. [2]) suggests an absence of the zero-bias DOS, which could be due to the limited signal-to-noise ratio.

In the main text (Fig. 3), we demonstrate that the $\mathbf{Q}_{CO}$ is consistent between bulk-sensitive RIXS and surface-sensitive STM. Supplementary Fig. 4 further shows this is true for the insulating Dy-Bi2212, where $\mathbf{Q}_{CO} = 0.32 \pm 0.03$ r.l.u. (Supplementary Fig. 4c), in agreement with the RIXS result (Fig. 2c in the main text). Note that (1) Because it is technically challenging to perform STM on insulating cuprates, the area of the $p = 0, 04$ sample is small (15×15 nm^2, see Fig. 2f); thus, the CO signal in the Fourier transformation (FT) image (Supplementary Fig. 4a) is weak. (2) To extract the $\mathbf{Q}_{CO}$ we take the FT image at $E = 150$ meV (Supplementary Fig. 4b) as a reference for the Bragg peak ($q_{AN} = 1$).

To mitigate the STM set-point effect, bias voltages of the $p = 0.04$ and $p = 0.06$ samples are set to -500 mV and -300 mV (see Methods), respectively. Similar to that reported by ref. [3], the CO wavevector is found prominent in the positive energy window (see Supplementary Figures 5 (a,b)). Moreover, at the negative set-point voltages, the current maps are featureless (Supplementary Figures 5 (c,d)), further demonstrating a negligible effect of the set-point effect on the CO signal.

Supplementary Fig. 6 plots together the PG map and the current ratio maps $R(|E|) = I(+E)/I(-E)$ at a high $E = 150$ meV, the latter facilitates the analysis of the tunneling rate asymmetry [4]. It can be visualized from the 'R-map' that there is a unidirectional maze-like (or 'electronic glass' [4]) pattern along the Cu-O bond direction pervading spatial locations where the PG is small and CO is well-developed (see Supplementary Fig. 3). In fact, this maze-like pattern has been proposed to be a generic feature of PG that breaks both the translational [4] and C4-rotational [5] symmetries and justifies our assignment of PG and its intertwining with CO.

3. The rationality of the two-phonon fitting model

With improved energy resolution, RIXS has the ability to simultaneously detect Cu-O bond stretching (BS) and out-of-plane bond buckling (BB) phonons [6–9]. In the context of our experiment, the energy resolution is $\Delta E = 36$ meV, and the dispersionless BB phonon has average energy ~ 35 meV (see below), making it reliable to address the information of both phonon branches.

Supplementary Fig. 7 demonstrates the necessity of exploiting two phonons in our fitting model. From an unbiased view like that reported in ref. [7], we respectively fit the energy gain region ($-0.06 \sim 0$ eV) and the high energy tail ($0.15 \sim 0.5$ eV, mostly paramagnon) of the raw data (e.g., Supplementary Fig. 7a), using a resolution-limited Gaussian and an antisymmetric Lorentzian convoluted with the energy resolution. The low-energy inelastic spectral weight can be obtained by subtracting the above two components from the raw data, which unambiguously reveals two peaks centered around 70 meV (black-shaded) and 35 meV (red-shaded). Therefore, we use a two-phonon model (Supplementary Fig. 7b and Methods) throughout our work, which gives a nearly perfect fitting result and negligible 'softening' at both branches.

Next, we compare our methodology with previous reported fitting models exploiting only BS phonon. For consistency, the elastic peak is fixed to a resolution-limited Gaussian function. The first model fits the low-energy inelastic region with a Lorentzian convoluted with the energy resolution [10] (Supplementary Fig. 7c). It fails to capture the

BS phonon peak position at small $\mathbf{q}_{//}$ where the spectral intensity is not very strong (but still evident). At larger $\mathbf{q}_{//}$ especially near the $\mathbf{Q}_{CO}$ (0.30 r.l.u.), the Lorentzian does not work well at energy scale ~ 30 meV corresponding to the BB phonon. Worse still, the Lorentzian is so broad (in order to fit the lower energy part) that the elastic and paramagnon peaks have been suppressed significantly, which may give rise to inaccurate conclusions. The same dilemma exists in other one-phonon models exploiting either anti-Lorentzian [11, 12] (see Supplementary Fig. 7e) or width-variable Gaussian function [13] (see Supplementary Fig. 7g). In any case, the subtracted RIXS spectra shown in Supplementary Figs. 7d, f, h still display two peak features, like those in Supplementary Fig. 7a.

4. Fitting results

Using the two-phonon fitting model, we decomposed the full dataset (Supplementary Fig. 2) into CO, BB phonon, and BS phonon intensity maps, as displayed in Supplementary Fig. 8. The quasi-elastic region (lower panel) of each figure was integrated to generate Fig. 5a of the main text. The BB phonon intensity (middle panel) of each figure was integrated to generate Supplementary Fig. 10a, which was further normalized to the background and shown as Fig. 5c of the main text. The BS phonon intensity (upper panel) of each figure was integrated to generate Fig. 5e of the main text, where all data points associated with the BS phonon overlap well since the thermal broadening effect at the ~ 70 meV energy scale is negligible. Notably, the measurement along the (H, H) direction shows no intensity anomaly of BB phonon when the CO is absent, see Supplementary Fig. 9.

Furthermore, we note that in ref. [7], two phonons are necessary to fit the RIXS spectra in NBCO cuprates. Notably, by comparing RIXS data of parent ($p \sim 0$, without CO) and optimally doped ($p \sim 0.16$, with CO) samples, the difference mainly manifests at wavevector larger than $\mathbf{Q}_{CO}$ and in energy coinciding with BB phonon, in concert with our results. On the other hand, the BS phonon remains unchanged at different dopings, which is also insensitive to CO and SC.

5. Why the enhanced BB phonon below T_c is statistically robust?

We have considered three different RIXS components at two different dopings, i.e., quasi-elastic CO, BB phonon, and BS phonon, each displaying systematic evolutions with as many as six temperatures and more than ten momentum transfers. Fig. 5d of the main text is a summarized plot of the above high-quality measurements, showing only one data point below T_c. However, this result is statistically robust for the following reasons.

First, the intensity anomaly of BB phonon is found at all temperatures and dopings (see Fig. 5b of the main text), centered around a wavevector slightly larger than $\mathbf{Q}_{CO}$. Such anomaly disappears when the CO is lacking, e.g., see refs. [7, 8] and Supplementary Fig. 9 along (H, H) direction. Hence, the phenomenon and its interpretation as an intricate interplay between CO excitations and EPC are robust. Second, even if we consider the single data point below T_c, the intensity jump appears at a range, not just a point of momentum transfer (see Fig. 5b of the main text). Third, for every momentum transfer in Fig. 5b of the main text, the data has been repeatedly taken with five independent measurements (see Supplementary Fig. 10b), thus being statistically robust.

6. Paramagnon excitations

Because our Dy-Bi2212 samples are heavily underdoped where the magnetic excitation is strong, it is worth studying whether the paramagnon plays a role in the CO, as suggested before by RIXS studies on $La_{1.875}Ba_{0.125}CuO_4$ [14], optimally doped Bi2201 [15] and electron-doped cuprates [16]. We use the linear horizontal (π) polarization of the incident X-ray to enhance the paramagnon signal due to its spin-flip nature [17].
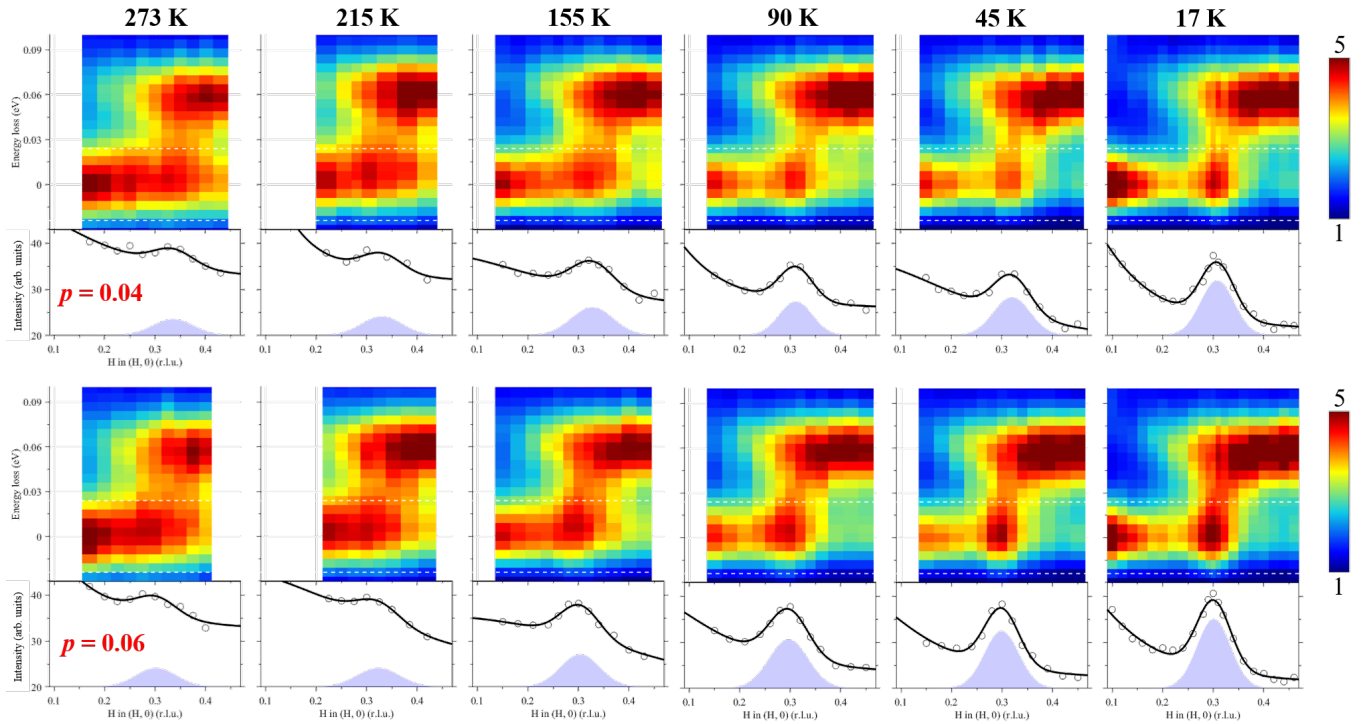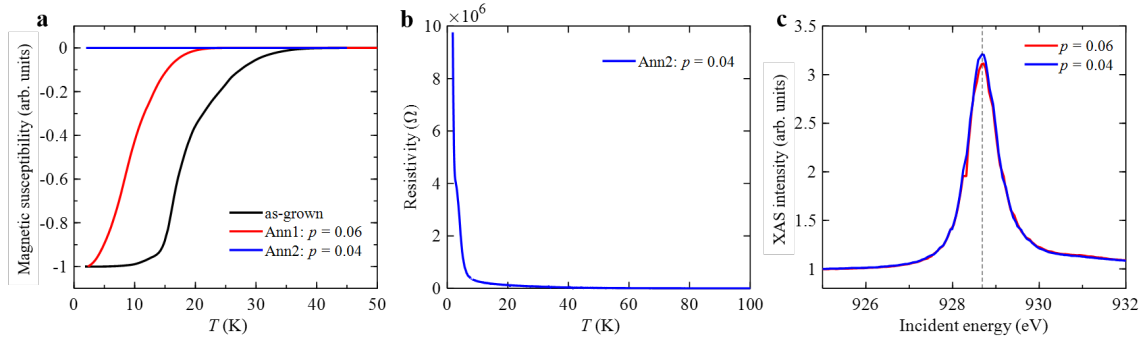
Supplementary Fig. 11a and 11b are the RIXS intensity maps taken in the $p = 0.04$ and $p = 0.06$ samples, respectively, which have been normalized to the areas of dd excitations and reveal evident paramagnon excitations at energy scale above 0.1 eV. To facilitate the analysis similar to that shown in refs. [15, 17], we decompose each RIXS spectrum into five different contributions (Supplementary Fig. 11c): (1-3) resolution-limited Gaussians for the elastic peak, BB and BS phonon modes, (4) a damped harmonic oscillator function $\chi''(\omega) = \gamma\omega/[(\omega^2 - \omega_0^2)^2 + 4\gamma^2\omega^2]$ for the paramagnon, which gives the undamped frequency ω_0, damping factor γ, and the propagation frequency $\omega_p = \sqrt{\omega_0^2 - \gamma^2}$, (5) a smooth background for other inelastic components. The paramagnon dominates the high-energy spectral weight, and its characteristic energy scales (ω_0, γ, ω_p) are shown in Supplementary Fig. 11d. The dispersion and damping are nearly identical in the two dopings, except that the γ has an overall smaller value at the $p = 0.04$ sample, which agrees with the smooth doping evolution of paramagnon [17]. None of the energy scales display a softening behavior, as suggested by ref. [14]. Another study (ref. [16]) reports an intensity peak at ~ 0.25
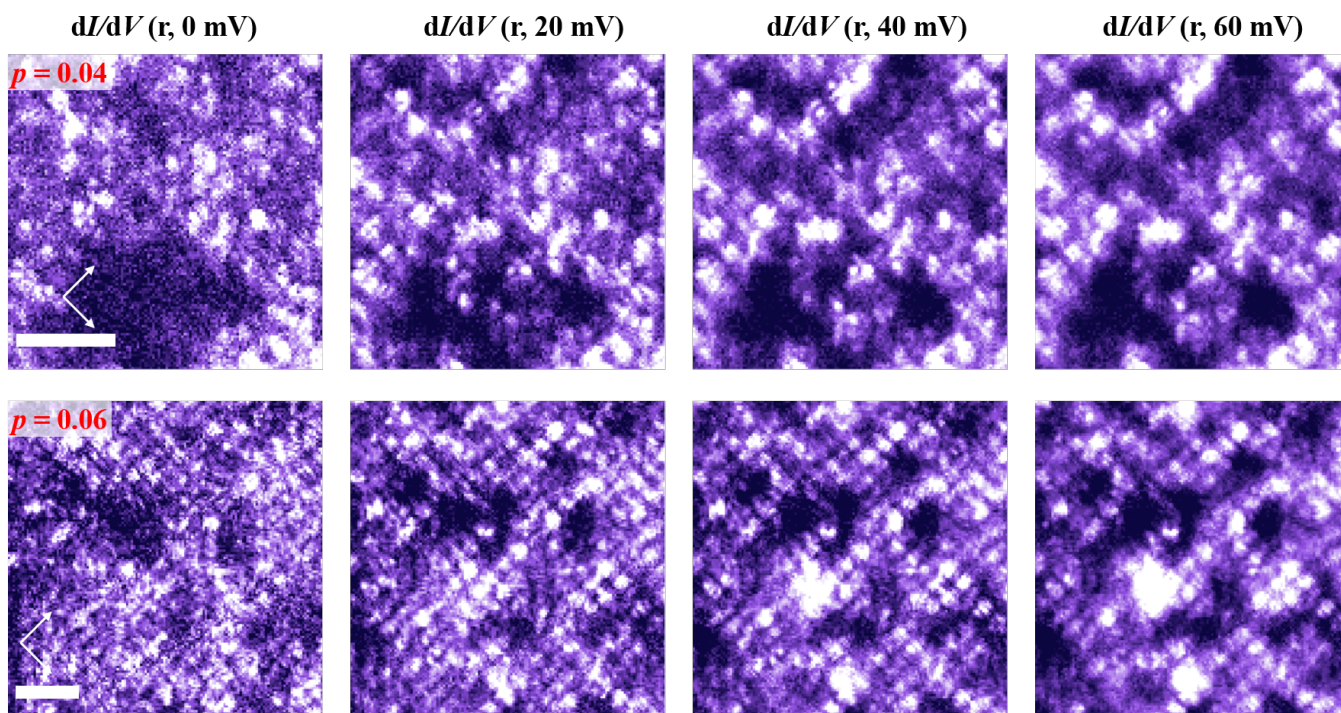
r.l.u. in electron-doped cuprates, which is close to its $\mathbf{Q}_{CO}$. A similar anomaly is observed here, but the peak is away from the $\mathbf{Q}_{CO} \sim 0.30$ r.l.u. of our samples. Therefore, no strong coupling is observed between magnetic excitations and the formation of short-range CO, at least in the heavily underdoped regime where the CO is incipient.

SUPPLEMENTARY REFERENCES

[1] Presland, M., Tallon, J., Buckley, R., Liu, R. & Flower, N. General trends in oxygen stoichiometry effects on Tc in Bi and Tl superconductors. *Phys. C* **176**, 95–105 (1991).

[2] Cai, P. *et al.* Visualizing the evolution from the mott insulator to a charge-ordered insulator in lightly doped cuprates. *Nat. Phys.* **12**, 1047–1051 (2016).

[3] da Silva Neto, E. H. *et al.* Ubiquitous Interplay between Charge Ordering and High-Temperature Superconductivity in Cuprates. *Science* **343**, 393-396 (2014).

[4] Kohsaka, Y. *et al.* An intrinsic bond-centered electronic glass with unidirectional domains in underdoped cuprates. *Science* **315**, 1380–1385 (2007).

[5] Lawler, M. J. *et al.* Intra-unit-cell electronic nematicity of the high-T_c copper-oxide pseudogap states. *Nature* **466**, 347–351 (2010).

[6] Devereaux, T. P. *et al.* Directly Characterizing the Relative Strength and Momentum Dependence of Electron-Phonon Coupling Using Resonant Inelastic X-Ray Scattering. *Phys. Rev. X* **6**, 041019 (2016).

[7] Braicovich, L. *et al.* Determining the electron-phonon coupling in superconducting cuprates by resonant inelastic x-ray scattering: Methods and results on $Nd_{1+x}Ba_{2-x}Cu_3O_{7-\delta}$. *Phys. Rev. Res.* **2**, 023231 (2020).

[8] Li, J. *et al.* Multiorbital charge-density wave excitations and concomitant phonon anomalies in $Bi_2Sr_2LaCuO_{6+}$. *Proc. Natl. Acad. Sci. U. S. A.* **117**, 16219–16225 (2020).

[9] Huang, H. Y. *et al.* Quantum Fluctuations of Charge Order Induce Phonon Softening in a Superconducting Cuprate. *Phys. Rev. X* **11**, 041038 (2021).

[10] Chaix, L. *et al.* Dispersive charge density wave excitations in $Bi_2Sr_2CaCu_2O_{8+\delta}$. *Nat. Phys.* **13**, 952–956 (2017).

[11] Lee, W. S. *et al.* Spectroscopic fingerprint of charge order melting driven by quantum fluctuations in a cuprate. *Nat. Phys.* **17**, 53–57 (2021).

[12] Lin, J. Q. *et al.* Strongly Correlated Charge Density Wave in $La_{2-x}Sr_xCuO_4$ Evidenced by Doping-Dependent Phonon Anomaly. *Phys. Rev. Lett.* **124**, 207005 (2020).

[13] Wang, Q. *et al.* Charge order lock-in by electron-phonon coupling in $La_{1.675}Eu_{0.2}Sr_{0.125}CuO_4$. *Sci. Adv.* **7**, 27 (2021).

[14] Miao, H. *et al.* High-temperature charge density wave correlations in $La_{1.875}Ba_{0.125}CuO_4$ without spin-charge locking. *Proc. Natl. Acad. Sci. U. S. A.* **114**, 12430–12435 (2017).

[15] Peng, Y. Y. *et al.* Magnetic excitations and phonons simultaneously studied by resonant inelastic x-ray scattering in optimally doped $Bi_{1.5}Pb_{0.55}Sr_{1.6}La_{0.4}CuO_{6+\delta}$. *Phys. Rev. B* **92**, 064517 (2015).

[16] da Silva Neto, E. H. *et al.* Coupling between dynamic magnetic and charge-order correlations in the cuprate superconductor $Nd_{2-x}Ce_xCuO_4$. *Phys. Rev. B* **98**, 161114 (2018).

[17] Peng, Y. Y. *et al.* Dispersion, damping, and intensity of spin excitations in the monolayer $(Bi,Pb)_2(Sr,La)_2CuO_{6+\delta}$ cuprate superconductor family. *Phys. Rev. B* **98**, 144507 (2018).
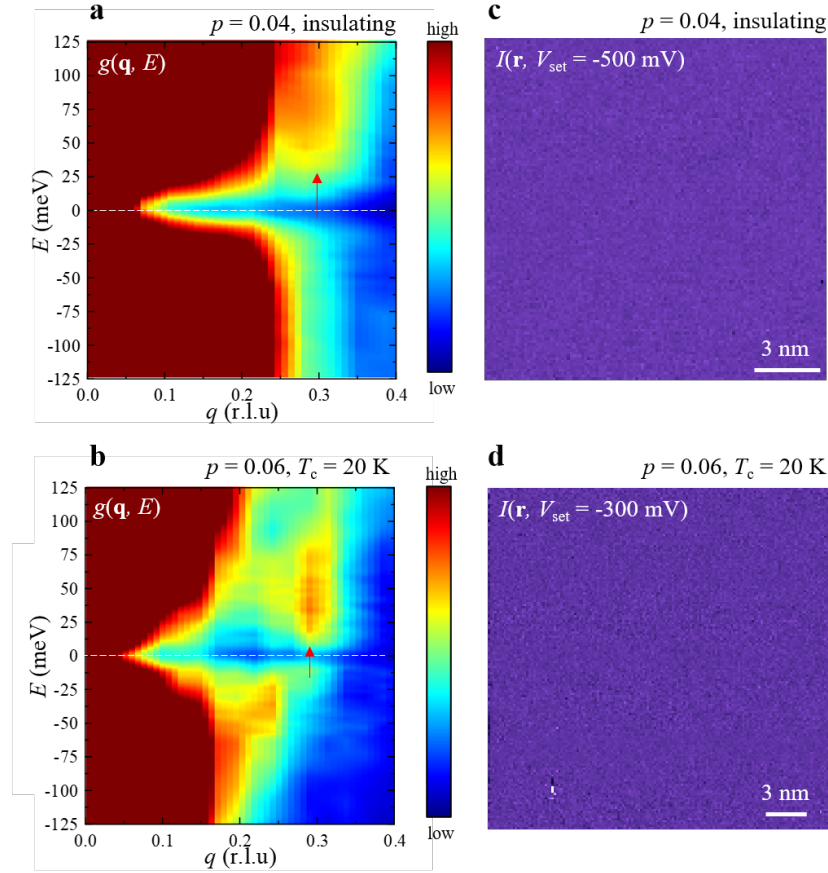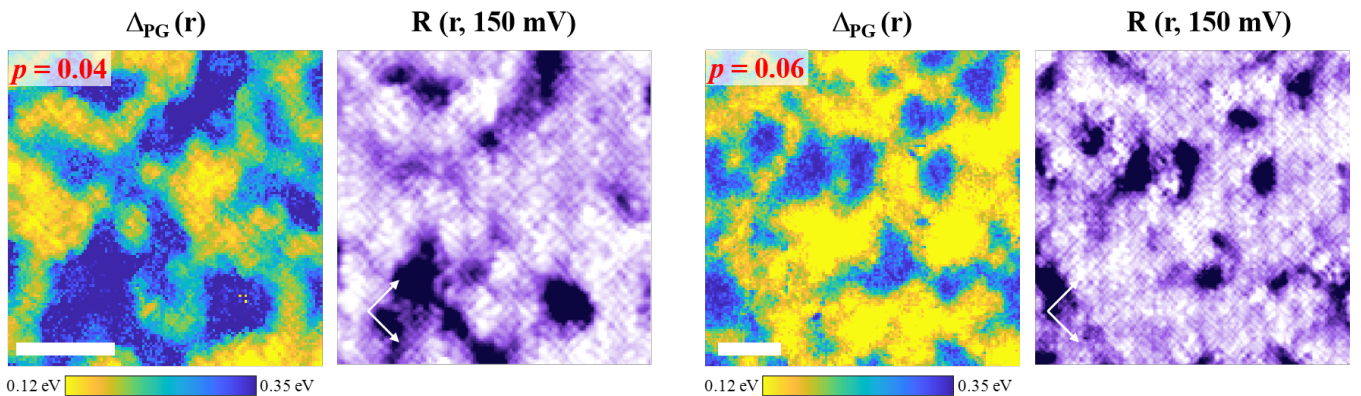
SUPPLEMENTARY FIGURES

Supplementary Figure 1. **Characterizations of the Dy-Bi2212 samples. a,** Magnetization curves for the as-grown (black) and vacuum-annealed (red and blue) Dy-Bi2212 crystals, obtained through ac-SQUID measurements. **b,** Resistance of another sample in the same batch (Ann2) as the $p = 0.04$ one, confirming the highly insulating behavior. **c,** XAS of the two samples studied, normalized to the spectral weight of the lower energy tail.

Supplementary Figure 2. **Raw RIXS intensity maps and CO.** The temperature dependence of the $p = 0.04$ (upper row) and $p = 0.06$ (lower row) data are shown, together with the integrated intensity profiles over the quasi-elastic region between the two white dashed lines. The black line and blue shaded area of each panel are the total fitting and CO peak of the profile (see Methods).

d*I*/d*V* (r, 0 mV)   **d*I*/d*V* (r, 20 mV)**   **d*I*/d*V* (r, 40 mV)**   **d*I*/d*V* (r, 60 mV)**

Supplementary Figure 3. **Non-dispersive CO revealed by the d*I*/d*V* maps.** The $p = 0.04$ (upper row) and $p = 0.06$ (lower row) data are in the same areas as Fig. 2f and Fig. 3a of the main text, respectively. White arrows denote the Cu-O bond directions. Scale bar: 5 nm.

a dI/dV(**q**, E=30 meV)

b dI/dV(**q**, E=150 meV)

c
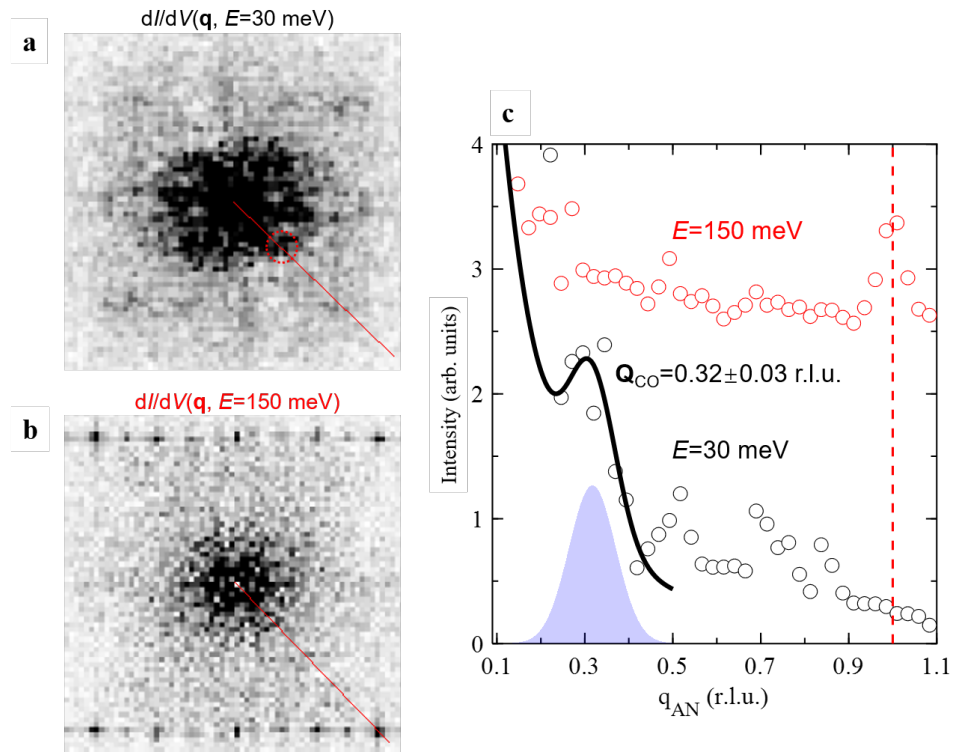
Supplementary Figure 4. **Fourier transformation (FT) result in the** $p = 0.04$ **sample. a,** FT of the real-space dI/dV map at $E = 30$ meV (Fig. 2f of the main text). The red dashed circles denote the CO peaks in the q-space. **b,** FT of the real-space dI/dV map at $E = 150$ meV, where the CO is absent but the Bragg peaks (red dashed circles) are evident. **c,** Line cuts along the antinodal direction (red line) of panels **a** and **b**, showing that $\mathbf{Q}_{CO} = 0.32$ r.l.u..

Supplementary Figure 5. **a,b,** The energy-dependent FFT plots of the $p = 0.04$ and $p = 0.06$ samples, respectively. The red arrow indicates the prominent charge order signal at the positive energy window [3], displaying the charge order wavevector at $Q \sim 0.3$ r.l.u.. **c,d,** The current map at set-point bias voltages on the $p = 0.04$ and $p = 0.06$ samples. The set-point effect is negligible, as shown by the featureless map.

Supplementary Figure 6. **Maze-like pattern generic of the PG.** In both the $p = 0.04$ (left panels) and $p = 0.06$ (right panels), the uni-directional maze-like pattern is strong at spatial locations where the PG magnitude is small. The intertwining of CO and PG is directly seen by comparing the CO pattern (Supplementary Figure 3), PG map $\Delta_{PG}(\mathbf{r})$ and symmetry-breaking R-map here. White arrows denote the Cu-O bond directions. Scale bar: 5 nm.
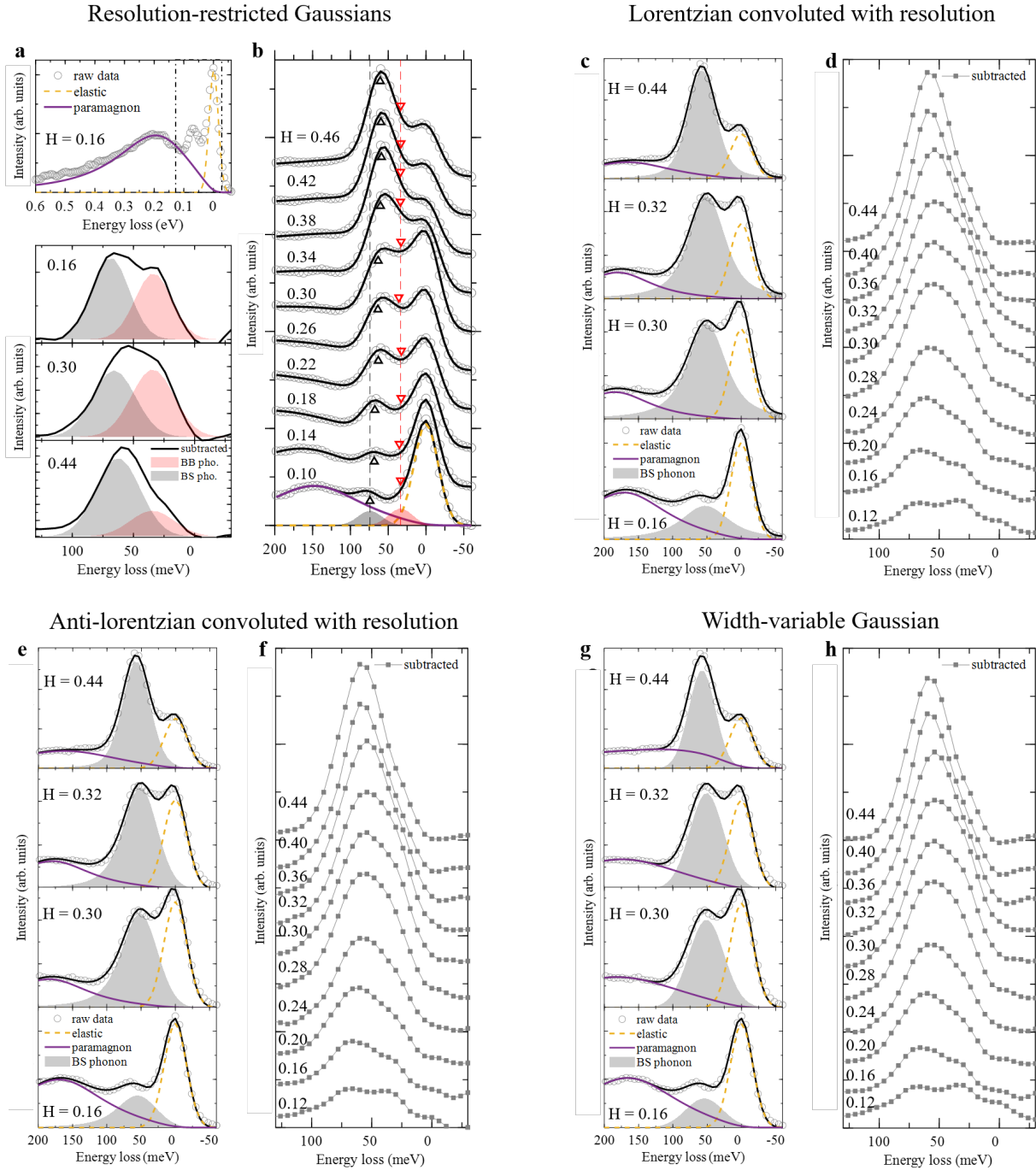
Supplementary Figure 7. **Comparison with one-phonon fitting models. a,** Unbiased method respectively fitting the elastic and paramagnon excitations, leaving behind two peak features in the low-energy inelastic region. **b,** The fitting results of our two-phonon model at different H. The black curves fit the RIXS data. The black and red triangles denote the fitted position of the BS and BB phonons, showing negligible softening. One-phonon models exploiting a Lorentzian convoluted with the energy resolution (**c**), or an antisymmetric Lorentzian convoluted with the energy resolution (**e**), or a width-variable Gaussian (**g**). The resulting low-energy inelastic spectra obtained by subtracting the elastic and paramagnon peaks from the raw data are shown in **d**, **f**, and **h** for each case.
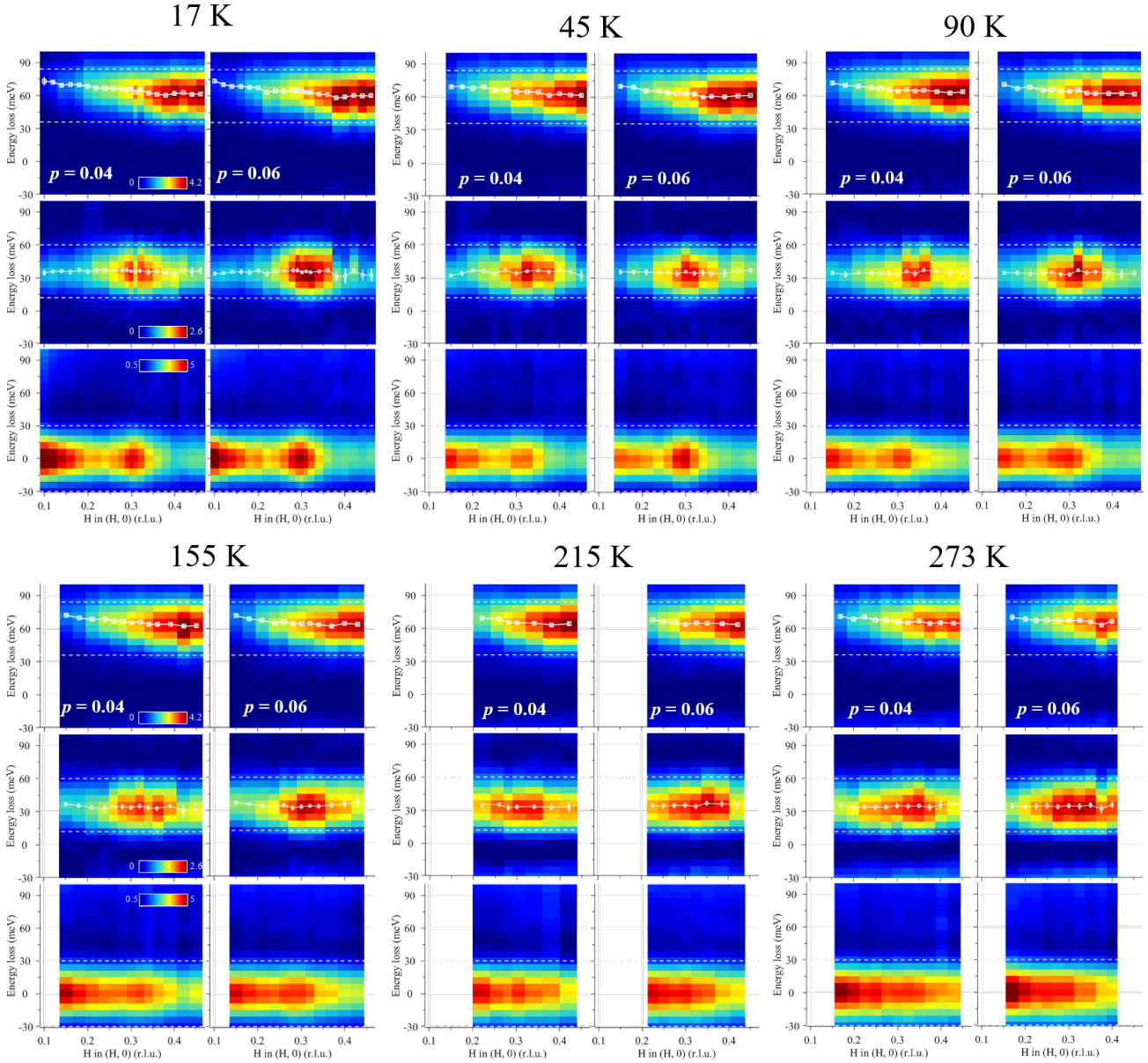
Supplementary Figure 8. **Decomposition of the RIXS excitations along (H,0) direction.** The maps are obtained by fitting the full dataset in Supplementary Figure 2 using the two-phonon model (Methods). Specifically, the CO component (lower panel of each figure) is taken by subtracting BB and BS phonon peaks from the raw data. The BB phonon map (middle panel) is taken by subtracting the elastic, BS phonon, and paramagnon peaks, and the BS phonon map (upper panel) is taken by subtracting the elastic, BB phonon, and paramagnon peaks from the raw data.
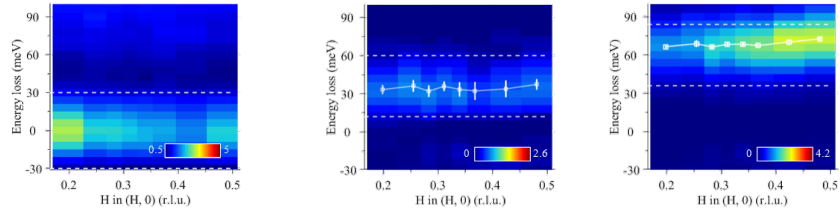

Supplementary Figure 9. **Decomposition of the RIXS excitations along (H, H) direction.** The maps are obtained using the same fitting procedure as Supplementary Figure 8.
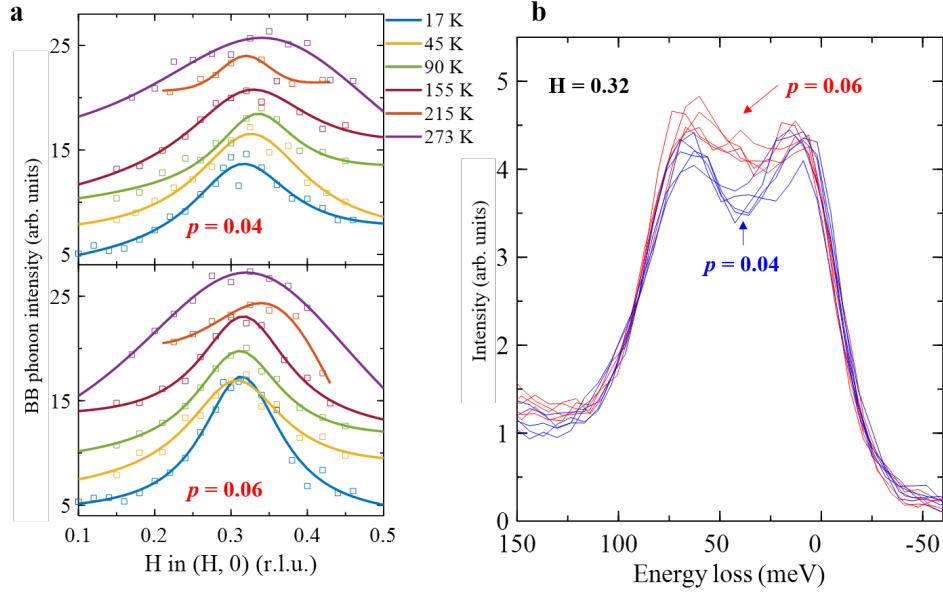
Supplementary Figure 10. **Intensity profiles of BB phonon and the repeatability. a** is obtained by integrating the BB phonon intensity maps (middle panels) of Supplementary Figure 8 and is offset for the same magnitude for clarity. The colored curve fits each profile using a Lorentzian function and linear background. **b** exemplifies the five individual measurements taken at H = 0.32 for the $p = 0.04$ (blue) and $p = 0.06$ (red) samples. The five curves shown here are averaged to obtain the data shown in Fig. 4d of the main text (middle panel).
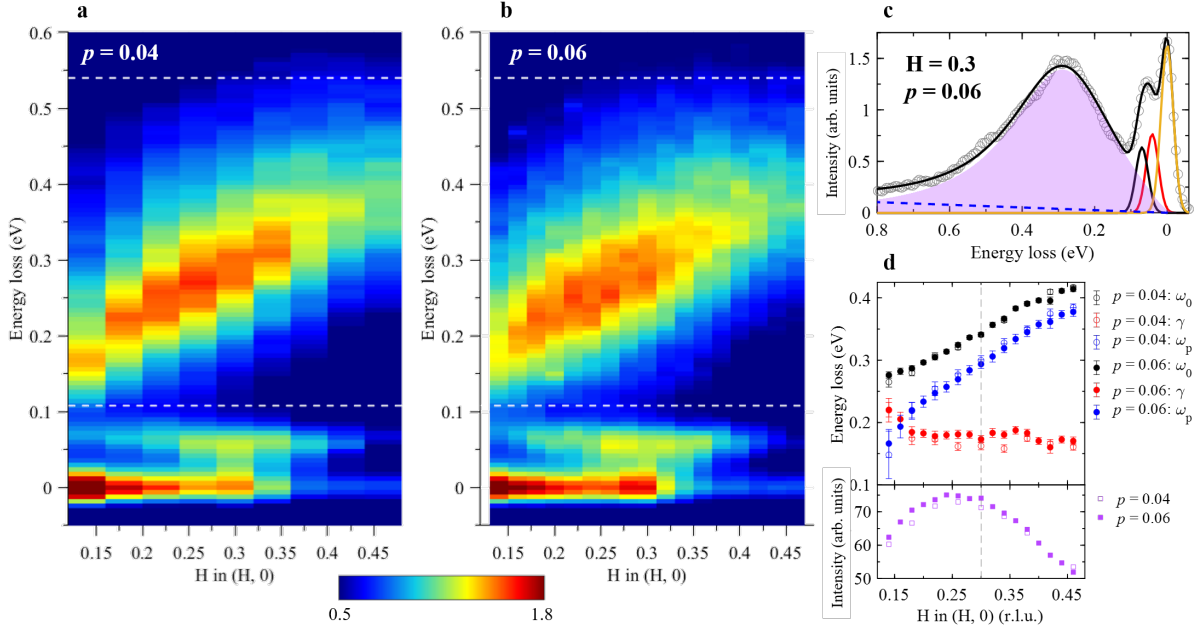
Supplementary Figure 11. **Paramagnon excitations with π polarization.** The RIXS intensity maps are shown in **a** for the $p = 0.04$ samples and in **b** for the $p = 0.06$ sample. **c,** An example demonstrating the fitting model. The purple shaded area highlights the paramagnon component. **d,** Upper panel: undamped frequency ω_0 (black), damping factor γ (red) and propagation frequency ω_p (blue) retrieved from the fitting. Lower panel: integrated paramagnon intensity between the white dashed lines in **a** and **b**.